A Scale-Selective Multilevel Method for Long-Wave Linear Acoustics

Stefan VATER[1], Rupert KLEIN[1], and Omar M. KNIO[2]

[1]Institute of Mathematics, Freie Universität Berlin, Berlin, Germany
e-mails: stefan.vater@math.fu-berlin.de (corresponding author),
rupert.klein@math.fu-berlin.de

[2]Department of Mechanical Engineering, Johns Hopkins University,
Baltimore, USA; e-mail: knio@jhu.edu

Abstract

A new method for the numerical integration of the equations for one-dimensional linear acoustics with large time steps is presented. While it is capable of computing the "slaved" dynamics of short-wave solution components induced by slow forcing, it eliminates freely propagating compressible short-wave modes, which are under-resolved in time. Scale-wise decomposition of the data based on geometric multigrid ideas enables a scale-dependent blending of time integrators with different principal features. To guide the selection of these integrators, the discrete-dispersion relations of some standard second-order schemes are analyzed, and their response to high wave number low frequency source terms are discussed. The performance of the new method is illustrated on a test case with "multiscale" initial data and a problem with a slowly varying high wave number source term.

Key words: linear acoustics, implicit time discretization, large time steps, balanced modes, multiscale time integration.

1 Introduction

Current operational general circulation models (GCMs) for global atmospheric flow simulations are based on the hydrostatic primitive equations (HPEs). These equations result from the full three-dimensional compressible flow equations in the limit of large

horizontal-to-vertical scale ratios. While this asymptotic limit suppresses vertically propagating sound waves, it does support long-wave horizontally traveling acoustic modes, the so-called "Lamb waves", and these are sometimes considered non-negligible for planetary-scale dynamics. Also, there are indications [Davies *et al.*, 2003] that effects of compressibility affect large-scale, deep internal wave modes of the atmosphere in a non-trivial fashion. Therefore, approximate "sound-proof" model equations, from which acoustic waves are eliminated entirely, may not provide an accurate representation of planetary scale flows. In contrast, current computational simulations of small-scale atmospheric processes, such as cloud formation, local storms, or pollutant transport on city-scales, are mostly based on analogues of the classical incompressible flow equations, i.e., on such "sound-proof" models [Lipps and Hemler, 1982; Durran, 1989; Grabowski, 1998].

Today, modern high-performance computing hardware is beginning to allow modelers to use grids with horizontal spacing in the range of merely a few kilometers even for planetary-scale simulations [see e.g., Ohfuchi *et al.*, 2004]. At such high resolution, the hydrostatic approximation breaks down, and one enters the scale range of sound-proof model applications. Although these issues are still under debate [Smolarkiewicz and Dörnbrack, 2008], keeping effects of compressibility in planetary-scale simulations seems desirable, and the challenge arises from combining large-scale compressible flow representations with essentially sound-proof modeling of the small scale dynamics.

In removing the hydrostatic constraint, and thus adopting the full compressible flow equations in a large-scale model, one is faced with considerable numerical difficulties. Explicit computational schemes, which would faithfully resolve sound perturbations at all wavelengths resolved by the model, are quite expensive, as they require very small time steps $\Delta t \sim \Delta x/c$, where Δx is the typical computational grid size, and c a characteristic sound speed. Alternatively, by adopting implicit time discretizations, one may overcome the time step limitations, but is then faced with a potentially undesirable numerical dispersion behavior of the resulting numerical schemes: most – if not all – existing implicit schemes of second or higher order of convergence achieve large time step stability by slowing down the short-wave acoustic modes. At the same time, some quite popular schemes essentially preserve their amplitude, which may seem desirable at a first glance, but can result in a source of nonlinear instabilities in practice (see Section 3.4 below).

To see this, consider a full-fledged atmospheric flow model which incorporates parametrization of subgrid scale diabatic effects, such as latent heat release from localized condensation. Local, small-scale heat release will set up non-zero flow divergences, and these are projected partially onto slow fake numerical acoustic modes. These modes will not disappear subsequently unless removed artificially, and they can influence the further flow evolution by interacting themselves with various subgrid scale parametrizations. A first-order implicit discretization, such as the implicit Euler scheme, will remove these short-wave fake acoustic modes, but it will also dampen or modify the long-wave modes in an undesired fashion.

Focusing on the representation of compressibility, the present work aims at a novel

discretization of the linearized acoustic equations that effectively overcomes these disadvantages of standard implicit discretizations. Ultimately, the scheme should

- ❏ eliminate freely propagating compressible short-wave modes that it cannot represent accurately due to spatio-temporal under-resolution,
- ❏ represent with second-order accuracy the "slaved" dynamics of short-wave solution components induced by slow forcing or arising in the form of high-order corrections to long-wave modes, and
- ❏ minimize dispersion for resolved modes.

To achieve these goals, the scheme incorporates

- a scale-dependent mode selection mechanism based on geometric multigrid ideas,
- scale-selective application of a proper discretization for the robust representation of balanced, slowly forced fast modes.

This paper reports first successful steps in this direction.

Multilevel schemes have been used elsewhere before, although they often have been only used for two or three different levels, in practice. Especially, they have been developed for the Navier-Stokes equation in the computation of turbulent flows [see e.g., Dubois *et al.*, 2004]. Another example is Dubois *et al.* [2005], where a spectral multilevel method for the computation of the shallow water equations is proposed. This scheme increases time step stability compared to an explicit method, while minimizing the dispersive error introduced by implicit discretizations.

After introducing the governing equations and their relevant properties in the next section, some standard time integration schemes used in meteorological applications are investigated in Section 3. On this basis, the construction of the new multiscale–multilevel method is discussed in Section 4. The performance compared to the standard schemes is studied in Section 5, and the article is closed by a final discussion.

2 Governing equations

The equations for one-dimensional linear acoustics are

$$
\begin{aligned}
m_t + p_x \quad &= 0 \ , \\
p_t + c^2 m_x &= q(t, \tfrac{x}{\varepsilon}) \ .
\end{aligned}
\tag{1}
$$

Here, $p = p(t, x)$ represents the pressure, $m = m(t, x)$ the momentum and c is the speed of sound. The source term $q(t, \tfrac{x}{\varepsilon})$, $\varepsilon \ll 1$, is chosen, such that it is slowly varying in time and has small scale variations in space. This source term could simulate the release of latent heat from localized condensation, for example.

System (1) has the dispersion relation

$$
\omega^2 - \kappa^2 c^2 = 0 \ ,
\tag{2}
$$

for traveling waves $(m, p)(t, x) = (m_0, p_0) \exp(i(\omega t - \kappa x))$. Thus $\omega(\kappa) = \pm c\kappa$, so that in the continuous system all waves travel with the same velocity, $c = \pm\omega/\kappa$, without dispersion. Furthermore, for $q \equiv 0$, eq. (1) implies the conservation law

$$\frac{\partial}{\partial t}\left(p^2 + c^2 m^2\right) + \frac{\partial}{\partial x}\left(2c^2 p\, m\right) = 0 \tag{3}$$

for the global pseudo-energy

$$E(t) = \int_\Omega p^2 + c^2 m^2 \,\mathrm{d}x \ . \tag{4}$$

Solutions of (1) are superpositions of a homogeneous part, which is characterized by freely traveling sound waves generated by initial and boundary conditions, and a part generated by the source term (particular solution). This particular solution inherits the scaling in ε given by the source term as we show in the subsequent asymptotic analysis. Focusing on the small-scale behavior of solutions, we consider the asymptotic expansion

$$m(t, x; \varepsilon) = m^{(0)}(t, \xi) + \varepsilon m^{(1)}(t, \xi) + \varepsilon^2 m^{(2)}(t, \xi) + \dots$$
$$p(t, x; \varepsilon) = p^{(0)}(t, \xi) + \varepsilon p^{(1)}(t, \xi) + \varepsilon^2 p^{(2)}(t, \xi) + \dots \tag{5}$$

with $\xi := \frac{x}{\varepsilon}$, $\varepsilon \ll 1$. Inserting this into (1), one obtains

$$m_t^{(0)} + \varepsilon m_t^{(1)} + \dots + \frac{1}{\varepsilon}\left(p_\xi^{(0)} + \varepsilon p_\xi^{(1)} + \dots\right) = 0 \ ,$$
$$p_t^{(0)} + \varepsilon p_t^{(1)} + \dots + \frac{c^2}{\varepsilon}\left(m_\xi^{(0)} + \varepsilon m_\xi^{(1)} + \dots\right) = q(t, \xi) \ , \tag{6}$$

and the leading order equations are $p_\xi^{(0)} \equiv 0$ and $m_\xi^{(0)} \equiv 0$. As a consequence,

$$p^{(0)} = p_0(t) \quad \text{and} \quad m^{(0)} = m_0(t) \ . \tag{7}$$

The next order equation for the pressure evolution is then given by

$$\frac{\mathrm{d}p_0}{\mathrm{d}t} + c^2 m_\xi^{(1)} = q(t, \xi) \ . \tag{8}$$

Integration over the domain $\Omega = [\xi_0, \xi_1]$ leads to

$$|\Omega|\frac{\mathrm{d}p_0}{\mathrm{d}t} + c^2\left(m^{(1)}(t, \xi_1) - m^{(1)}(t, \xi_0)\right) = \int_{\xi_0}^{\xi_1} q(t, \xi)\,\mathrm{d}\xi \ , \tag{9}$$

and considering, for simplicity, a periodic domain, where $m^{(1)}(t, \xi_1) = m^{(1)}(t, \xi_0)$, the zeroth order pressure and momentum equations read

$$\frac{\mathrm{d}p_0}{\mathrm{d}t} = \frac{1}{|\Omega|}\int_{\xi_0}^{\xi_1} q(t, \xi)\,\mathrm{d}\xi =: \bar{q}(t) \ ,$$
$$c^2 m_\xi^{(1)} = q(t, \xi) - \bar{q}(t) \qquad =: \tilde{q}(t, \xi) \ . \tag{10}$$

With the same arguments, one obtains $\frac{\mathrm{d}m_0}{\mathrm{d}t} = 0$, and $p_\xi^{(1)} \equiv 0$, i.e., $p^{(1)} = p_1(t)$, and the evolution equation for $p^{(1)}$ gives $p^{(1)} \equiv$ const. Therefore, the first non-trivial spatial variations of the pressure are described by $p^{(2)}$, and a closed system of equations is given by

$$
\begin{aligned}
m_t^{(1)} + p_\xi^{(2)} &= 0 \ , \\
c^2 m_\xi^{(1)} &= \tilde{q}(t, \xi) \ .
\end{aligned}
\tag{11}
$$

Differentiating the first equation with respect to ξ and the second with respect to t, one can see that the pressure is given by the elliptic equation

$$
-p_{\xi\xi}^{(2)} = m_{t\xi}^{(1)} = \frac{1}{c^2} \frac{\partial \tilde{q}}{\partial t} \ .
\tag{12}
$$

Assuming $m^{(0)} \equiv 0$, the asymptotic scaling in this regime is given by

$$
\begin{aligned}
m &\sim \varepsilon \ , \\
p - p_0(t) &\sim \varepsilon^2 \ ,
\end{aligned}
\tag{13}
$$

as $\varepsilon \to 0$. This scaling should be reproduced by a numerical scheme, especially, when $\Delta t \gg \frac{\Delta x}{c} = \frac{\varepsilon \Delta \xi}{c}$ which, in the present model problem, corresponds with large acoustic Courant numbers for the time integration. Furthermore, solutions that are only triggered by the source term should have the structure given by eq. (12) up to small perturbations. If we insert this scaling into the governing equations (1) (i.e., $x = \varepsilon\xi$, $m = \varepsilon\tilde{m}$ and $p = \varepsilon^2\tilde{p}$), the resulting system is

$$
\begin{aligned}
\tilde{m}_t + \tilde{p}_\xi \quad\ &= 0 \ , \\
\varepsilon^2 \tilde{p}_t + c^2 \tilde{m}_\xi &= q(t, \xi) \ ,
\end{aligned}
\tag{14}
$$

and one can see that the first term of the second equation is singular.

3 Implicit second-order staggered grid schemes

Here we describe the point of departure of the present developments, classical implicit second-order time integration schemes employing central differences on a staggered grid. The authors are aware of the fact that there are other popular discretizations such as multistage schemes. However, these methods usually require at least two linear systems to solve in order to achieve second order accuracy. Because of this additional cost per time step, we confine ourselves to schemes which only require the solution of one linear system per time step. We choose a staggered grid for simplicity only. Our key ideas should transfer directly to collocated grid arrangements as well.

3.1 Standard time integration schemes

The time integration schemes we investigate are the implicit trapezoidal rule and the BDF(2) scheme (Backward Differentiation Formula of second order). These are discretizations commonly used in meteorological applications [Durran, 2010]. Considering a semi-discretization in time we leave the choice of a spatial discretization open for the moment.

3.1.1 Implicit trapezoidal rule

In this discretization, the system in (1) is integrated in time from t^n to t^{n+1}, and the time integral on the right-hand side is approximated by the trapezoidal quadrature rule, so that

$$
\begin{aligned}
m^{n+1} - m^n &= -\frac{\Delta t}{2}\left(\frac{\partial p^n}{\partial x} + \frac{\partial p^{n+1}}{\partial x}\right) , \\
p^{n+1} - p^n &= -\frac{c^2 \Delta t}{2}\left(\frac{\partial m^n}{\partial x} + \frac{\partial m^{n+1}}{\partial x}\right) + \Delta t\, q^{n+1/2} .
\end{aligned}
\tag{15}
$$

Note that we do not specify how to compute the source term at this stage. The notation $q^{n+1/2}$ just indicates at which time level the source term would have to be evaluated to get a second order accurate approximation. To compute the pressure p at the new time step, one has to solve the Helmholtz problem

$$
p^{n+1} - \frac{c^2 \Delta t^2}{4}\frac{\partial^2 p^{n+1}}{\partial x^2} = p^n - c^2 \Delta t \frac{\partial m^n}{\partial x} + \frac{c^2 \Delta t^2}{4}\frac{\partial^2 p^n}{\partial x^2} + \Delta t\, q^{n+1/2} .
\tag{16}
$$

The update for m is then given by

$$
m^{n+1} = m^n - \frac{\Delta t}{2}\left(\frac{\partial p^n}{\partial x} + \frac{\partial p^{n+1}}{\partial x}\right) .
\tag{17}
$$

The trapezoidal rule is equivalent to the implicit midpoint rule, if the equations are linear. Since it only incorporates known values from the previous time step in the computation of the new time step, it is a one-step method. Furthermore, the method is *A*-stable and (for linear problems) symplectic [Hairer *et al.*, 2006]. Thus, for vanishing source term, $q \equiv 0$, it preserves the pseudo-energy from (4) up to machine accuracy.

3.1.2 BDF(2) rule

The BDF(2) scheme is one of the simplest methods of the so-called *Backward Differentiation Formulas (BDF)*. It is a two-step method, in which the left-hand side is approximated by the derivative of a parabola at t^{n+1}, which interpolates the solution at times t^{n-1}, t^n and t^{n+1}. The discretization of eq. (1) is then given by

$$
\begin{aligned}
\frac{\frac{3}{2}m^{n+1} - 2m^n + \frac{1}{2}m^{n-1}}{\Delta t} &= -\frac{\partial p^{n+1}}{\partial x} , \\
\frac{\frac{3}{2}p^{n+1} - 2p^n + \frac{1}{2}p^{n-1}}{\Delta t} &= -c^2 \frac{\partial m^{n+1}}{\partial x} + q^{n+1} .
\end{aligned}
\tag{18}
$$

Rearranging terms, p at the new time step is obtained by the solution of the elliptic problem

$$p^{n+1} - \frac{4c^2 \Delta t^2}{9} \frac{\partial^2 p^{n+1}}{\partial x^2} = \frac{4}{3} p^n - \frac{1}{3} p^{n-1} - c^2 \Delta t \left(\frac{8}{9} \frac{\partial m^n}{\partial x} - \frac{2}{9} \frac{\partial m^{n-1}}{\partial x} \right) + \frac{2}{3} \Delta t \, q^{n+1} \,, \quad (19)$$

and the update for m is given by

$$m^{n+1} = \frac{4}{3} m^n - \frac{1}{3} m^{n-1} - \frac{2}{3} \Delta t \frac{\partial p^{n+1}}{\partial x} \,. \quad (20)$$

3.2 Super-implicit scheme (extreme BDF)

As can be seen in the result of the asymptotic analysis of the governing equations (14), the time derivative of the pressure becomes singular in the limit $\varepsilon \to 0$. Thus, in the following scheme, the pressure equation is discretized by a so-called super-implicit scheme. Super-implicit methods are of more implicitness than the so-called implicit formulas in the sense that the approximation of the (highest) time derivative in the equation does not involve values at the new time level, i.e., only the approximation of the right-hand side involves new time level evaluations. They were first introduced by Fukushima [1999] for the application in celestial mechanics.

With the super-implicit discretization of the pressure equation as it is done in the following, we achieve one crucial property that led us to consider these schemes in the first place: since the time derivative will be discretized backwards in time based on the already known pressure data, the pressure equation effectively becomes a Poisson equation with two source terms. The first results from the pressure time derivative and represents the non-acoustic effects of compressibility with second order accuracy. The second source term is due to the divergence of the momentum flux and appears in the same form also in the pressure projection equation for incompressible flows [see e.g., Schneider *et al.*, 1999; Vater and Klein, 2009; Klein, 2009]. This discretization therefore allows us to make an immediate connection to incompressible or, more generally, sound-proof flow solvers.

In our discretization, the pressure evolution is interpolated by a parabola as in the BDF(2) scheme, but this time the interpolation points are t^{n-2}, t^{n-1} and t^n, which leads to

$$\frac{\frac{5}{2} p^n - 4 p^{n-1} + \frac{3}{2} p^{n-2}}{\Delta t} = -c^2 \frac{\partial m^{n+1}}{\partial x} + q^{n+1} \,. \quad (21)$$

The momentum equation is discretized as in the BDF(2) scheme. Rearranging terms, one obtains

$$-\frac{2c^2 \Delta t^2}{3} \frac{\partial^2 p^{n+1}}{\partial x^2} = -\left(\frac{5}{2} p^n - 4 p^{n-1} + \frac{3}{2} p^{n-2} \right) - c^2 \Delta t \left(\frac{4}{3} \frac{\partial m^n}{\partial x} - \frac{1}{3} \frac{\partial m^{n-1}}{\partial x} \right) + \Delta t \, q^{n+1} \,.$$
$$(22)$$

Thus, this discretization results in the solution of an elliptic equation as ordinary implicit schemes do, but this time it is a Poisson equation instead of a Helmholtz equation for the pressure at the new time step. The update for the momentum is again (20).

Note, however, that this discretization has an "inverse stability constraint" in that it becomes unstable for too small time steps with respect to a fixed mode (see Section 3.4 below).

3.3 Space discretization

As we have stated above, the space discretization is done using a staggered grid in this study. On this grid, the pressure variables are node centered, i.e., $p_{j+1/2}$, $j = 0, 1, \ldots, M$, where M is the number of nodes. The momentum variables, on the other hand, are cell centered, i.e., m_j, $j = 1, 2, \ldots, M$. Standard approximations for the first derivatives of the pressure and momentum are given in this context by

$$\left.\frac{\partial p}{\partial x}\right|_{x_j} \approx \frac{p_{j+1/2} - p_{j-1/2}}{\Delta x} \quad \text{and} \quad \left.\frac{\partial m}{\partial x}\right|_{x_{j+1/2}} \approx \frac{m_{j+1} - m_j}{\Delta x} \ . \tag{23}$$

The matching approximation for the second derivative of the pressure is then given by

$$\left.\frac{\partial^2 p}{\partial x^2}\right|_{x_{j+1/2}} \approx \frac{p_{j+3/2} - 2p_{j+1/2} + p_{j-1/2}}{\Delta x^2} \ . \tag{24}$$

Using these discretizations, the elliptic problems as in eqs. (16), (19) and (22) result in a linear system for the unknown $(p_{j+1/2})$. The system is then solved using a conjugate gradient algorithm in the applications described below.

3.4 Dispersion relations and balanced modes

To be able to quantify the behavior of the numerical discretizations described above, the *discrete-dispersion relations* of these schemes will be investigated in the following. Furthermore, the capability of the schemes to reproduce the balanced modes as described by the asymptotic analysis of Section 2 will be discussed.

The discrete-dispersion relation of a method is obtained by substituting a traveling wave solution of the form

$$\phi_j^n = \hat{\phi} \, e^{\mathrm{i}(kj\Delta x - \omega n\Delta t)} \tag{25}$$

into the finite-difference formula and solving for ω [Durran, 2010]. By separating the frequency into its real and imaginary parts, $\omega = \omega_\mathrm{r} + \mathrm{i}\omega_\mathrm{i}$, one obtains

$$\phi_j^n = \hat{\phi} \, e^{\omega_\mathrm{i} n\Delta t} \, e^{\mathrm{i}(kj\Delta x - \omega_\mathrm{r} n\Delta t)} = \hat{\phi} \, |A|^n e^{\mathrm{i}(kj\Delta x - \omega_\mathrm{r} n\Delta t)} \ . \tag{26}$$

For a scalar equation, the computation of the imaginary part of ω is equivalent to a von Neumann stability analysis. The amplification factor $|A|$ determines how much the mode grows or dissipates per time step. The real part ω_r, on the other hand, describes
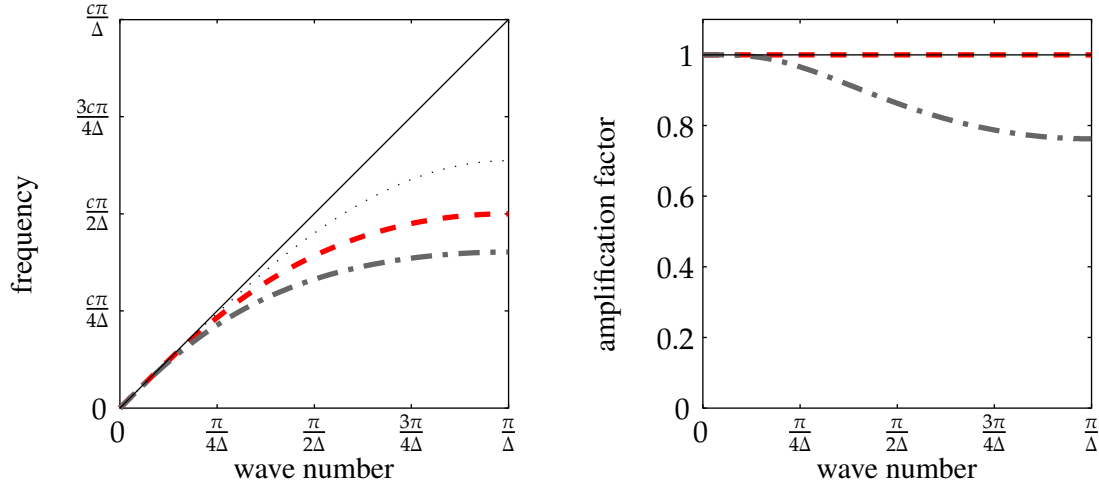
Figure 1: Discrete-dispersion relations for the trapezoidal (dashed) and the BDF(2) rules (dot-dashed) applied to the linear acoustic equations using $\mathrm{cfl} = 1$. Dispersion relation for continuous system is displayed as black line. Discrete-dispersion relation for the limiting case $\mathrm{cfl} \to 0$ is given as dotted line.

the phase speed error. For a system of equations the same analysis can be carried out, although, in order to obtain stability of the scheme, the requirement that the amplification factor be less than or equal to unity is merely a necessary condition in general.

The discrete-dispersion relation of the trapezoidal rule applied to the linear acoustic equations on a staggered grid is given by

$$(\xi - 1)^2 + \left(\mathrm{cfl} \cdot \sin\left(\frac{k\Delta x}{2} \right) \right)^2 (\xi + 1)^2 = 0 \; , \tag{27}$$

where $\xi := e^{-i\omega\Delta t}$ and $\mathrm{cfl} = \frac{c\Delta t}{\Delta x}$ is the Courant-Friedrichs-Lewy (CFL) number [Courant *et al.*, 1928]. Solving for ω one obtains for the real part

$$\omega_\mathrm{r} = \pm \frac{2}{\Delta t} \arctan\left(\mathrm{cfl} \cdot \sin\left(\frac{k\Delta x}{2} \right) \right) \tag{28}$$

and for the amplification factor $|A| \equiv 1$. Thus, essentially, the frequency depends not only on the wave number, as in the continuous case, but it is also a function of the CFL number. The derivation of the discrete-dispersion relation for the BDF(2) scheme follows the same route.

Figures 1 and 2 show the discrete-dispersion relations for the trapezoidal and the BDF(2) rules applied to the linear acoustic equations for different CFL numbers. We find that both schemes slow down modes at almost all wave numbers. This behavior is amplified the higher the wave number and the higher the CFL number, with the
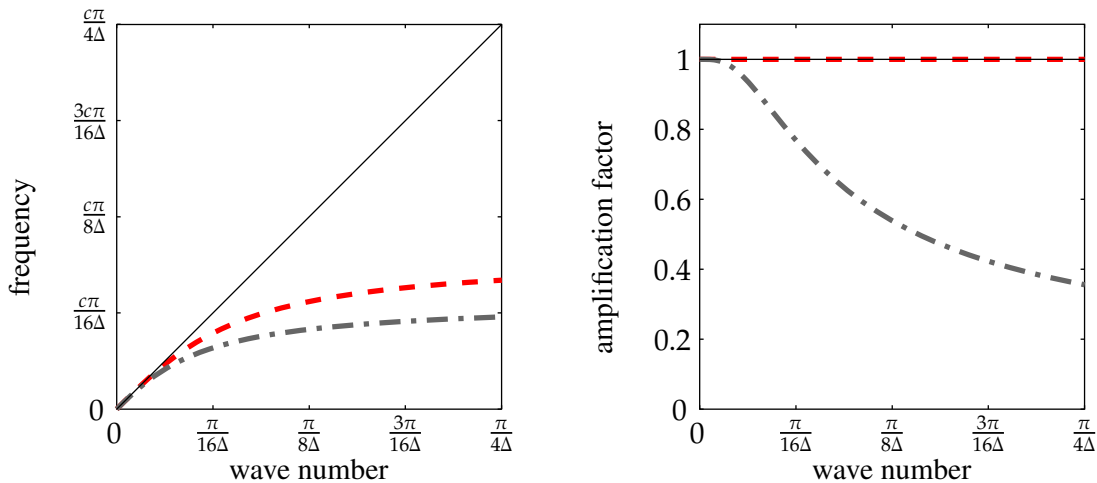
Figure 2: Discrete-dispersion relations for the trapezoidal (dashed) and the BDF(2) rules (dot-dashed) applied to the linear acoustic equations using cfl = 10. Dispersion relation for continuous system is displayed as black line.

trapezoidal rule featuring the smaller phase speed error of the two throughout. Furthermore, in contrast to the BDF(2) scheme, the trapezoidal scheme is free of numerical dissipation.

It has to be emphasized that the slowdown of high (acoustic) modes is an immanent property of implicit methods. By looking at the limit cfl → 0 one obtains for both, the trapezoidal rule and the BDF(2) scheme, the dispersion relation

$$\omega_{\mathrm{r}}^{\mathrm{lim}} = \pm \frac{2c}{\Delta x} \sin\left(\frac{k\Delta x}{2}\right) \ . \tag{29}$$

As one can see in Figure 1, where the limiting case is plotted by a dotted line, only modes with a wavelength of about 10 grid points and more are advected at a reasonable speed.

For the super-implicit scheme, we have not found an analytical expression for the discrete-dispersion relation. The amplification factor obtained by numerical simulations is displayed in Figure 3 for cfl = 10. The graph illustrates the inverse stability behavior of this scheme in that the amplification factor for small wave numbers is greater than one at a given time step size. For smaller time steps (resp. CFL numbers) the amplification factor further increases, making the scheme more unstable. The figure further shows, however, that modes with sufficiently high wave numbers are damped.

Concerning the balanced mode we are interested here in how accurately the various schemes maintain the asymptotic balance for the case of slow, short-wave forcing, and whether they are capable of regaining the balance after some perturbation of the system. As stated above, the source term is assumed to be slowly varying in time in our setting,
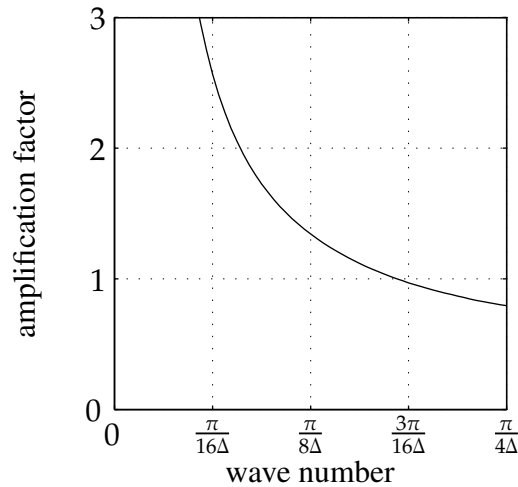
Figure 3: Amplification factor for the super-implicit scheme applied to the linear acoustic equations using $\mathrm{cfl} = 10$.

so that the balance is described by

$$c^2 m_x = q\left(t, \tfrac{x}{\varepsilon}\right) \quad \text{and} \quad p \equiv 0 \tag{30}$$

up to small perturbations introduced by the variation in time of the source term. The capability to regain the balanced state should be possible for finite time steps, where it is successively approached over a number of time steps. Furthermore, the scheme should reproduce the balanced state in one time step by letting the step going to infinity. These conditions are related to the concepts of *A*- and *L*-stability in the mathematical literature of numerical methods for stiff problems [see, e.g., Deuflhard and Bornemann, 2002]. However, here we have to deal with an oscillatory equation, which is not stiff in the (classical) sense, in that some eigenvalues would have large negative real parts.

The first property, the ability of the method to relax to the balanced state successively, manifests itself through the amplification factor from the discrete-dispersion relations given above. If the amplification factor is less than unity, the scheme damps out a sudden perturbation and relaxes back to the balanced state. This is true for the BDF(2) scheme, whereas the trapezoidal rule has an amplification factor of unity for all wave numbers so that any short-wave perturbation that the scheme interprets as an acoustic mode will maintain its amplitude subsequently.

Considering the limit $\Delta t \to \infty$, one obtains for the trapezoidal rule the relations

$$\frac{c^2}{2}\left(\frac{\partial m^n}{\partial x} + \frac{\partial m^{n+1}}{\partial x}\right) = q^{n+1/2} \quad \text{and} \quad \frac{\partial p^{n+1}}{\partial x} = -\frac{\partial p^n}{\partial x} \ . \tag{31}$$

This reflects the behavior described above that any perturbation cannot dissipate. The first derivatives of pressure and momentum essentially oscillate around the balanced

state. In case of the BDF(2) and the super-implicit schemes the situation is quite different. In the limit $\Delta t \to \infty$ one obtains for both methods

$$c^2 \frac{\partial m^{n+1}}{\partial x} = q^{n+1} \quad \text{and} \quad \frac{\partial p^{n+1}}{\partial x} = 0 \; . \tag{32}$$

Thus, the schemes achieve balance in a single, sufficiently large, time step. This behavior is characteristic to backward differences formulas by construction [Deuflhard and Bornemann, 2002].

As a consequence, the practitioner is faced with the following problem: On the one hand, one would like to minimize dispersion and preserve the amplitude of well resolved modes. For this purpose the trapezoidal rule seems to be the best suited one of the schemes described above. On the other hand, the solution should rapidly relax to the balanced mode in case of short wave number forcing. For this purpose the backward differencing formulas are better suited. In the next section, we present a strategy for combining the two aspects into one single, scale-dependent numerical time integrator.

4 Multilevel method for long-wave linear acoustics

By "long-wave" we denote here highly resolved acoustic modes that oscillate very slowly in comparison with the shortest acoustic modes that could potentially be represented on the grid. The goal is to provide a discretization that guarantees the following: given a time step, the scheme will automatically filter all acoustic modes from the initial data that have characteristic frequencies which are not resolved in time, whereas all sufficiently long waves with lower frequencies get to be resolved and accurately computed. Thus we intend to avoid the dichotomy between either damping all acoustic modes or accepting spurious, slowly moving short-wave modes outlined in the introduction.

4.1 General idea

Assume that we have scale dependent splittings of the pressure and momentum fields, i.e.,

$$p = \sum_{\nu=0}^{\nu_M} p^{(\nu)} \quad \text{and} \quad m = \sum_{\nu=0}^{\nu_M} m^{(\nu)} \tag{33}$$

where these splittings have still to be determined. Ideally, this could be a quasi-spectral or wavelet decomposition, splitting p and m into (local) high wave number and low wave number components. Furthermore, we assume we have two time discretizations of the equations for linear acoustics, which are linear in p^{n+1} and m^{n+1}. In general, they can be written as

$$S_1^p(p^{n+1}, m^{n+1}, p^n, m^n, p^{n-1}, m^{n-1}, \dots) = 0 \; ,$$
$$S_1^m(p^{n+1}, m^{n+1}, p^n, m^n, p^{n-1}, m^{n-1}, \dots) = 0 \; , \tag{34}$$

and

$$S_2^p(p^{n+1}, m^{n+1}, p^n, m^n, p^{n-1}, m^{n-1}, \dots) = 0 \; ,$$
$$S_2^m(p^{n+1}, m^{n+1}, p^n, m^n, p^{n-1}, m^{n-1}, \dots) = 0 \; , \tag{35}$$

where S_i^p represents the discretization for the pressure equation, and S_i^m the one for the momentum equation. A convex combination of the two schemes with scale dependent weights results in the scheme

$$\sum_{\nu=0}^{\nu_M} \mu_\nu S_1^p(p^{(\nu),n+1}, \dots) + (1 - \mu_\nu) S_2^p(p^{(\nu),n+1}, \dots) = 0 \ ,$$
$$\sum_{\nu=0}^{\nu_M} \mu_\nu S_1^m(p^{(\nu),n+1}, \dots) + (1 - \mu_\nu) S_2^m(p^{(\nu),n+1}, \dots) = 0 \ . \tag{36}$$

In order to solve for p^{n+1} and m^{n+1}, one has to combine the two equations in (36) to obtain an elliptic equation for p^{n+1}. This results, as in the schemes described above, in a Helmholtz problem, but this time with a scale dependent operator.

As a first example consider the blending of the implicit trapezoidal rule with the BDF(2) scheme. For the trapezoidal rule, we have

$$p^{(\nu),n+1} - \frac{c^2 \Delta t^2}{4} p_{xx}^{(\nu),n+1} = p^{(\nu),n} - c^2 \Delta t \, m_x^{(\nu),n} + \frac{c^2 \Delta t^2}{4} p_{xx}^{(\nu),n} + \Delta t \, q^{(\nu),n+1/2} \ ,$$
$$m^{(\nu),n+1} = m^{(\nu),n} - \frac{\Delta t}{2} \left(p_x^{(\nu),n} + p_x^{(\nu),n+1} \right) \ , \tag{37}$$

and for the BDF(2) scheme

$$p^{(\nu),n+1} - \frac{4c^2 \Delta t^2}{9} p_{xx}^{(\nu),n+1} = \frac{4}{3} p^{(\nu),n} - \frac{1}{3} p^{(\nu),n-1}$$
$$- c^2 \Delta t \left(\frac{8}{9} m_x^{(\nu),n} - \frac{2}{9} m_x^{(\nu),n-1} \right) + \frac{2}{3} \Delta t \, q^{(\nu),n+1} \ , \tag{38}$$
$$m^{(\nu),n+1} = \frac{4}{3} m^{(\nu),n} - \frac{1}{3} m^{(\nu),n-1} - \frac{2}{3} \Delta t \, p_x^{(\nu),n+1} \ .$$

Taking the μ-dependent convex combination of the two schemes and summing over the scales results in

$$p^{n+1} - c^2 \Delta t^2 \sum_{\nu=0}^{\nu_M} \left(\frac{\mu_\nu}{4} + \frac{4(1 - \mu_\nu)}{9} \right) p_{xx}^{(\nu),n+1} = \sum_{\nu=0}^{\nu_M} \left(\mu_\nu \text{RHS}_{\text{TRA}}^{p,(\nu)} + (1 - \mu_\nu) \text{RHS}_{\text{BDF2}}^{p,(\nu)} \right) \ , \tag{39}$$

where

$$\text{RHS}_{\text{TRA}}^{p,(\nu)} = p^{(\nu),n} - c^2 \Delta t \, m_x^{(\nu),n} + \frac{c^2 \Delta t^2}{4} p_{xx}^{(\nu),n} + \Delta t \, q^{(\nu),n+1/2} \ ,$$
$$\text{RHS}_{\text{BDF2}}^{p,(\nu)} = \frac{4}{3} p^{(\nu),n} - \frac{1}{3} p^{(\nu),n-1} - c^2 \Delta t \left(\frac{8}{9} m_x^{(\nu),n} - \frac{2}{9} m_x^{(\nu),n-1} \right) + \frac{2}{3} \Delta t \, q^{(\nu),n+1} \ . \tag{40}$$

The momentum update then reads

$$m^{n+1} = \sum_{\nu=0}^{\nu_M} \mu_\nu \left[m^{(\nu),n} - \frac{\Delta t}{2} \left(p_x^{(\nu),n} + p_x^{(\nu),n+1} \right) \right] +$$
$$(1 - \mu_\nu) \left[\frac{4}{3} m^{(\nu),n} - \frac{1}{3} m^{(\nu),n-1} - \frac{2}{3} \Delta t \, p_x^{(\nu),n+1} \right] \ . \tag{41}$$

13

Note that we do not specify the discretization of the source term q, and we assume at this stage that we could integrate this term exactly.

In a second example, we combine the trapezoidal rule with the super-implicit (extreme BDF) scheme described above. The resulting update is given by

$$\sum_{\nu=0}^{\nu_M} \mu_\nu p^{(\nu),n+1} - \frac{c^2 \Delta t^2}{4} p_{xx}^{n+1} = \sum_{\nu=0}^{\nu_M} \left(\mu_\nu \text{RHS}_{\text{TRA}}^{p,(\nu)} + (1 - \mu_\nu) \text{RHS}_{\text{EBDF}}^{p,(\nu)} \right) \,, \qquad (42)$$

where

$$\begin{aligned}
\text{RHS}_{\text{TRA}}^{p,(\nu)} &= p^{(\nu),n} - c^2 \Delta t\, m_x^{(\nu),n} + \frac{c^2 \Delta t^2}{4} p_{xx}^{(\nu),n} + \Delta t\, q^{(\nu),n+1/2} \,, \\
\text{RHS}_{\text{EBDF}}^{p,(\nu)} &= \frac{3}{8} \left(-\frac{5}{2} p^n + 4 p^{n-1} - \frac{3}{2} p^{n-2} - c^2 \Delta t \left(\frac{4}{3} m_x^n - \frac{1}{3} m_x^{n-1} \right) + \Delta t\, q^{n+1} \right) \,.
\end{aligned} \qquad (43)$$

The update for the momentum is again given by (41).

Note that if the scale dependent splitting (33) is not a direct splitting (i.e., the grid functions for different scales are coupled with each other; an example is the splitting described in the next section), the elliptic problems for each scale are coupled to each other and cannot be solved separately. Instead, the Helmholtz problem (39) (resp. (42)) must be solved as a whole. The main difference between the two examples is that the difference operator acting on the pressure variables in the first example incorporates the multiscale information in its discrete Laplacian part (second term of LHS in eq. (39)), whereas in the second example it appears in the Helmholtz part (first term of LHS in eq. (42)).

4.2 Scale splitting

To define the operators in the scale-dependent discretizations, the quasi-spectral decompositions of the pressure and momentum fields have to be carefully specified. Furthermore, we will see that the two splittings cannot be defined independently, but have to satisfy certain relationships.

First, we discuss the decomposition of the pressure field. In a second step we derive the appropriate momentum decomposition. In order to define the grid hierarchy, we assume that the total number of grid cells in the domain is a power of 2. Then, a coarser grid is obtained by eliminating every second grid node and thus, by merging two adjacent cells. In our current approach the restriction and prolongation operators used in standard multigrid algorithms are utilized to define the space decomposition. One of the most commonly used operator pairs for finite difference approximations (and in a slightly modified way also for finite element approximations) is the *full weighting* (restriction) and the *linear interpolation* (prolongation) [Trottenberg *et al.*, 2001]. They can be defined by their stencil. The full weighting is given by

$$R^{(\nu)} = \frac{1}{4} \begin{bmatrix} 1 & 2 & 1 \end{bmatrix} \,, \qquad (44)$$
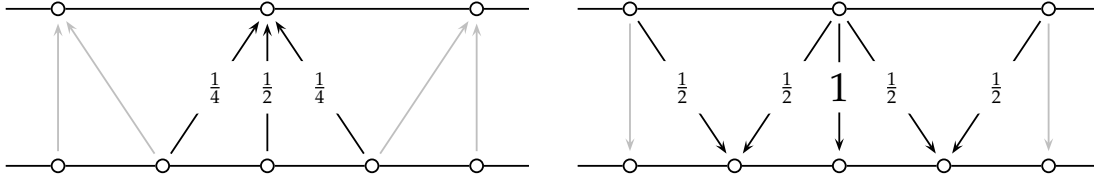
Figure 4: One-dimensional versions of full weighting (left) and linear interpolation (right) operators known from standard finite difference geometric multigrid. Arrows indicate mappings between grid functions associated with grid nodes.
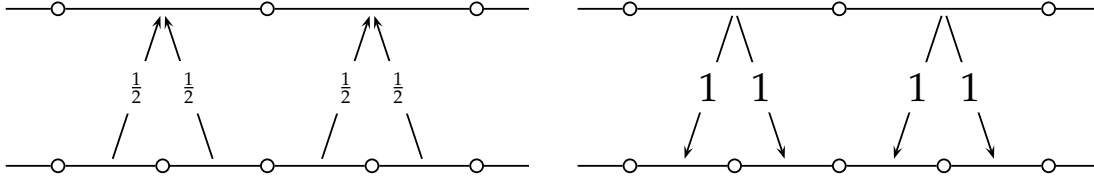
Figure 5: One-dimensional versions of restriction (left) and prolongation (right) operators known from standard finite volume geometric multigrid. Arrows indicate mappings between grid functions associated with grid cells (instead of with grid nodes as in Figure 4).

which means that a variable on the coarse grid node (at grid level (ν)) is derived by averaging over the values at the same node and the two adjacent nodes on the fine grid (at grid level $(\nu + 1)$) with the weights given in the stencil above (see also Figure 4, left). The linear interpolation from grid level (ν) to grid level $(\nu + 1)$ is given by

$$P^{(\nu)} = \frac{1}{2} \begin{bmatrix} 1 & 2 & 1 \end{bmatrix} . \tag{45}$$

This means that the pressure at grid nodes living on the fine grid level, which have a common coarse grid node, obtain the same value as on the coarse grid. The values at grid nodes in between are computed by the average of the values of the adjacent grid nodes (Figure 4, right).

Other alternatives are also possible. A common restriction/prolongation pair used in finite volume approximations for cell centered variables is given by

$$\tilde{R}^{(\nu)} = \frac{1}{2} \begin{bmatrix} 1 & 1 \end{bmatrix} \quad \text{and} \quad \tilde{P}^{(\nu)} = \begin{bmatrix} 1 & 1 \end{bmatrix} . \tag{46}$$

Here, the value for the coarse grid cell is computed by simply averaging over the two corresponding small cells on the fine grid, and the values for the fine grid cells are obtained by just copying the value from the corresponding coarse grid cell (cf. Figure 5).

The scale splitting is now defined as follows. Let φ be a grid function, which is

decomposed into parts $\varphi^{(\nu)}$ living on the associated grid levels:

$$\varphi = \sum_{\nu=0}^{\nu_M} \varphi^{(\nu)} \; . \tag{47}$$

Then, the grid function on the coarsest level is obtained by the operation

$$\varphi^{(0)} = \left(R^{(0)} \circ R^{(1)} \circ \cdots \circ R^{(\nu_M-1)} \right) \varphi \tag{48}$$

and the grid functions on finer levels are computed by

$$\varphi^{(\nu)} = \left(I - P^{(\nu-1)} \circ R^{(\nu-1)} \right) \circ \left(R^{(\nu)} \circ R^{(\nu+1)} \circ \cdots \circ R^{(\nu_M-1)} \right) \varphi \; . \tag{49}$$

On a staggered grid the splitting in the momentum field cannot be the same as the one for the pressure. Since the momentum variable is cell centered, only transfer operators as in (46) are applicable. The splitting has to be chosen such that only the portion of the pressure associated with the grid level (ν) enters the update for the momentum on the same grid level. Revisiting equation (41), we see that only first derivatives of the pressure at different time levels enter the update. Therefore, the splitting in the momentum must match the splitting in $\partial p / \partial x$ induced by the p-splitting. This results in (see Appendix)

$$R^{(\nu)} = \frac{1}{8} \begin{bmatrix} 1 & 3 & 3 & 1 \end{bmatrix} \; , \tag{50}$$

and

$$P^{(\nu)} = \begin{bmatrix} 1 & 1 \end{bmatrix} \; . \tag{51}$$

To complete the description of the new scheme, we need to define the weighting function μ_ν. Generally, this choice is not restricted besides the requirement that the resulting scheme should be stable. In the current implementation we have chosen

$$\mu_\nu = \min \left(1, \frac{\nu_M - \nu}{\lfloor \log_2 \text{cfl} \rfloor} \right) \; , \tag{52}$$

where $\lfloor \cdot \rfloor$ means rounding towards minus infinity. Thus, μ_ν is chosen such that the scheme in eq. (36) associates the standard implicit trapezoidal scheme with all pressure modes corresponding to coarse grids with grid-CFL number cfl ≤ 1 ($\mu_\nu = 1$), while we nudge the discretization towards BDF(2) or super-implicit for pressure modes living on grids with cfl > 1 ($\mu_\nu < 1$).

4.3 Interaction between time and space discretizations

To analyze the properties of the Helmholtz operator associated with the new scheme we have computed the corresponding matrix. By applying the operator to the unit vector $e_i = (\delta_{ij})_{j=1,\dots,n}$, one obtains the i-th column of the matrix. In Figure 6, the sparsity pattern for the resulting matrices of the blended trapezoidal/BDF(2) scheme (left) and
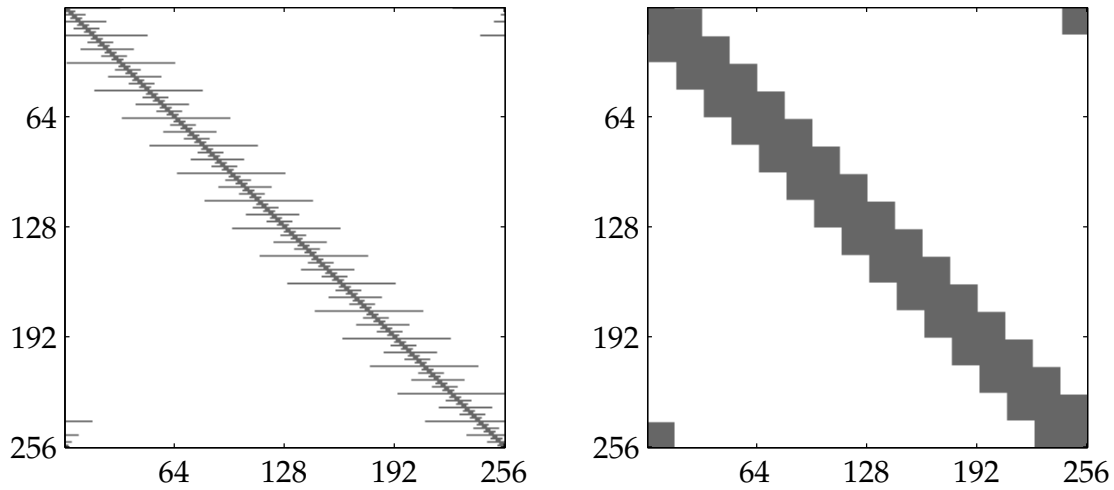
Figure 6: Sparsity pattern for the resulting matrices of blended schemes, domain with 256 grid cells and five grid levels. Left: trapezoidal/BDF(2); right: trapezoidal/super-implicit.

the blended trapezoidal/super-implicit scheme (right) are displayed for a domain with 256 grid cells. Obviously, the matrices do not have the same typical tridiagonal pattern as the blended base schemes. In contrast, the different time integration schemes for each scale influence the effective space discretization. However, the deviations in the matrix entries from those resulting from the single-scale fine grid time integrator have a relative order of magnitude of at most one percent.

Note that the pattern also depends on the weighting function μ_ν and the number of grid levels. The displayed results are obtained for five grid levels and μ_ν changing linearly from the coarsest level ($\mu_0 = 1$) to the finest level ($\mu_{\nu_M} = 0$). Thus, we see the maximum with respect to non-zero matrix entries for this number of levels. For μ_ν as defined above and a Courant-Friedrichs-Lewy number cfl $= 10$, the band width of the matrix is slightly reduced. The differences in the pattern between the two versions of the new scheme is essentially due to the fact that in case of the blended trapezoidal/BDF(2) scheme the multiscale information is hidden in the Laplacian part of the operator, and in case of the blended trapezoidal/super-implicit scheme it is hidden in the Helmholtz part.

Also, the sparsity pattern suggests that the elliptic problem with such an operator cannot be solved with standard numerical methods. The authors are currently working on solution methods that borrow ideas from multigrid methods for elliptic problems.

5 Numerical Results

The new scheme is applied to two test cases, and the results are compared to those of the standard reference methods. The first test case explores the desired property to

treat short-wave data differently compared to long-wave data. For this purpose, the scheme is initialized with "multiscale" initial data and no source term is present. In a second test case, the ability of the scheme to relax to a balanced state is analyzed. In order to do this, a source term with the appropriate scaling is introduced. In both test cases, a sound speed of $c = 1$ is chosen. For the new scheme, we always use five grid levels.

5.1 Multiscale initial data

In this test case, we compare the previously described numerical schemes by applying them to either pure long-wave initial data, or "multiscale" initial data in a periodic domain $x \in [0, 1]$. The relationship between pressure and momentum is chosen in such a way that one obtains a right running acoustic simple wave. The pure long-wave data is given by

$$p(x, 0) = p_0(x - x_0) \quad \text{and} \quad m(x, 0) = p(x, 0)/c \,, \tag{53}$$

where

$$p_0(x) = \exp\left(-\left(\frac{x}{\sigma_0}\right)^2\right) \tag{54}$$

with $x_0 = 0.75$ and $\sigma_0 = 0.1$, and the "multiscale" initial data is

$$p(x, 0) = p_0(x - x_0) + p_1(x - x_1) \quad \text{and} \quad m(x, 0) = p(x, 0)/c \,, \tag{55}$$

where p_0 is defined as above and

$$p_1(x) = p_0(x) \cos(kx/\sigma_0) \tag{56}$$

with $x_1 = 0.25$ and $k = 7 \cdot 2\pi$ (see Figure 7).

The schemes are applied to this initial data on a grid with 512 cells (i.e., $\Delta x = 1/512$) and a Courant-Friedrichs-Lewy number cfl = 10. They are compared at a final time $t_{\text{end}} = 3.0$, which is equivalent to 154 time steps. At this time the exact solution is identical to the initial data, and the wave has traveled three times across the domain.

The implicit trapezoidal rule described in Section 3.1 produces the results in Figure 8. Here, and in the following, only pressure is displayed, whenever the momentum field is essentially the same. The results show what has already been revealed theoretically by the discrete-dispersion relation for large time steps. The scheme achieves large-CFL stability by slowing down the short-wave components of the solution. In the single-scale example, the consequence of this numerical dispersion error is a slight dispersion of the Gaussian pulse which generates new artificial extrema, and slightly slows down the wave. When run over longer times, this trend continues and the Gaussian pulse decomposes into an essentially uncorrelated superposition of Fourier modes of various length scales.

For the multiscale initial data, the insuing error is much more dramatic. The numerical scheme slows down the short-wave component of the solution to nearly zero phase speed. While the long-wave pulse in Figure 8 (right), has passed the domain three times, as it
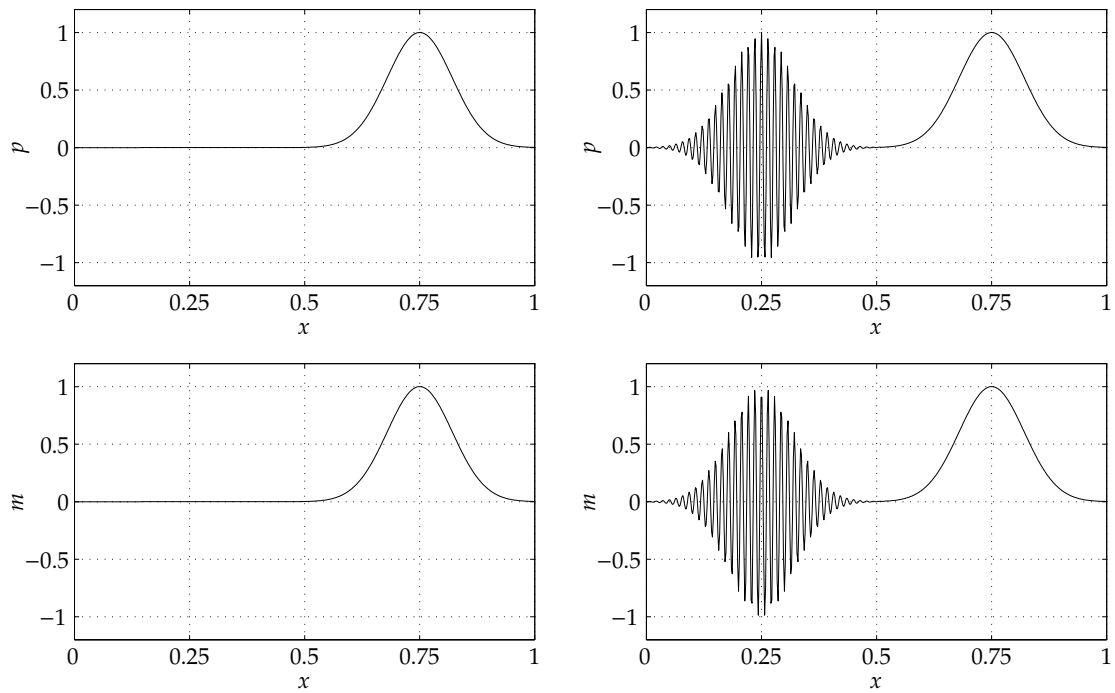
Figure 7: Initial conditions with single-scale pure long-wave data (left) and "multiscale" data (right). Top row: pressure, bottom row: momentum.
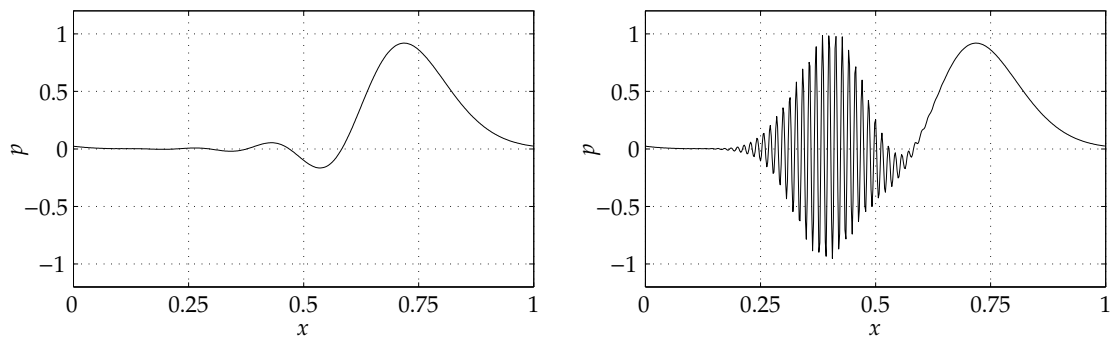
Figure 8: Numerical solution (pressure) using the trapezoidal rule on a grid with 512 cells and $\mathrm{cfl} = 10$ at time $t_{\mathrm{end}} = 3$. Left: results obtained with single scale data; right: results obtained with "multiscale" data.
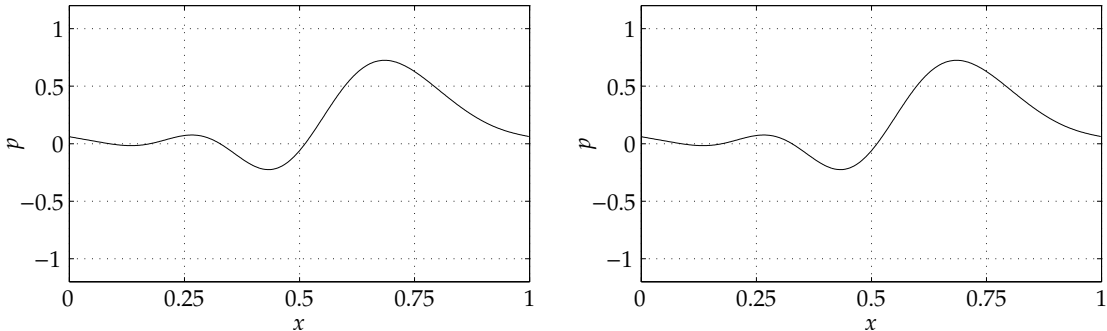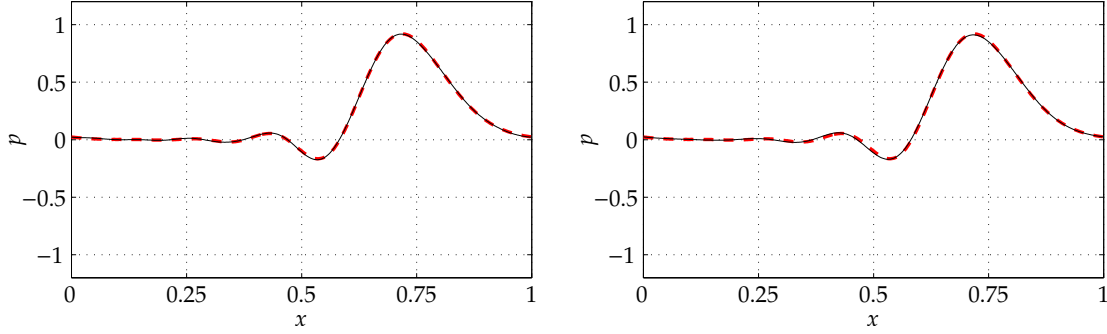
Figure 9: Numerical solution (pressure) using the BDF(2) scheme on a grid with 512 cells and cfl = 10 at time $t_{\mathrm{end}} = 3$. Left: results obtained with single scale data; right: results obtained with "multiscale" data.

should, the short-wave oscillations have essentially stayed in place. Furthermore, their amplitude has not diminished.

Clearly, such a behavior, when extrapolated to global atmospheric flow simulations, would be unacceptable. Not only would the planetary scale Lamb waves be slightly distorted, but any small-scale divergence induced by one of the ubiquitous diabatic source terms in an atmosphere model would potentially set up stationary, short-wave, fake numerical standing waves (see also second test case). In interaction with the parametrizations of various physical subgrid-scale processes, nota bene the physics of moisture, these short-wave modes will likely produce non-trivial erroneous consequences for the further flow evolution.

The BDF(2) scheme displays a different behavior, as seen in Figure 9. According to the discrete-dispersion relation, the scheme has considerably more dispersion than the trapezoidal rule. Furthermore, the damping of the scheme results in a smaller final amplitude, even for the long-wave data. On the short scales, the damping is so high that at the final time $t_{\mathrm{end}} = 3$ the simulation started with "multiscale" data (Figure 9, right) is indistinguishable from the one started with pure long-wave data (Figure 9, left). Thus, the scheme is able to balance the short-wave modes that are not resolved in time, but it pays the price of simultaneously damping and dispersing the long scales.

As stated above, in case of the blended scheme one tries to combine the capability of the trapezoidal rule to relatively well resolve the long-wave acoustics with a scheme which filters the highly oscillatory short-wave data in an appropriate fashion. The results of the simulations using the blended schemes with multiscale initial data are displayed in Figure 10. We applied the trapezoidal rule in combination with the BDF(2) scheme (left) and the trapezoidal rule together with the super-implicit method (right). For comparison, the result of using the trapezoidal rule applied only to the long-wave initial data is also shown in the plots (dashed line). As one can see, the latter is nearly identical to the results using the blended schemes. This is the desired behavior. The short-wave data is damped out in such a way that only the long-wave data is left after

Figure 10: Numerical solution (pressure) using the blended schemes on a grid with 512 cells and $\mathrm{cfl} = 10$ at time $t_{\mathrm{end}} = 3$ (black line). Left: results obtained with the blended trapezoidal/BDF(2) scheme; right: results obtained with the blended trapezoidal/super-implicit scheme. For comparison, the result of trapezoidal rule obtained with only long-wave initial data is plotted as dashed line.

some time. On the other hand, the long-wave data is integrated as good as one could hope when using a second-order method.

5.2 Balanced modes in presence of a source term

To evaluate the ability of the new scheme to relax to balanced states after some perturbation, a source term of the form

$$q\left(t, \tfrac{x}{\varepsilon}\right) = q(t, \xi) = \sin\left(\omega\, t\right) \tilde{q}(\xi - \xi_0)\;, \tag{57}$$

where

$$\tilde{q}(\xi) = \left(\frac{2 + \lambda^2 \sigma^2}{\lambda^2 \sigma^2} \sin(\lambda\,\xi) + \frac{4}{\lambda \sigma^2} \cos(\lambda\,\xi)\xi - \frac{4}{\lambda^2 \sigma^4} \sin(\lambda\,\xi)\xi^2\right) \exp\left(-\left(\frac{\xi}{\sigma}\right)^2\right) \tag{58}$$

with $\omega = 2\pi$, $\xi_0 = 0.5$, $\sigma = 0.1$ and $\lambda = 16 \cdot 2\pi$ is introduced. By choosing $\varepsilon \ll 1$, a source term of the desired form is obtained. To obtain a well resolved source term in space, we do our computations on the domain $\xi \in [0, 1]$ and a grid with 256 cells (i.e., $\Delta \xi = 1/256$). Thus, the computational domain and the spatial extent of the source term is scaled with ε. Furthermore, periodic boundary conditions are applied and as initial conditions we set $p(0, x) \equiv m(0, x) \equiv 0$. In the computations, the source term is integrated analytically over one time step.

As a result of the asymptotic analysis in Section 2, pressure should scale with ε^2 and momentum with ε in this case, and as a result of eq. (12) they should, up to higher order perturbations, have the form

$$p_{\mathrm{asy}}(t, \xi) = \varepsilon^2 \omega \cos\left(\omega\, t\right) \tilde{p}(\xi - \xi_0) \tag{59}$$

21

with

$$\tilde{p}(\xi) = \frac{1}{\lambda^2} \sin(\lambda \xi) \exp\left(-\left(\frac{\xi}{\sigma}\right)^2\right) , \tag{60}$$

and

$$m_{\mathrm{asy}}(t, \xi) = \varepsilon \sin(\omega t) \, \tilde{m}(\xi - \xi_0) , \tag{61}$$

where

$$\tilde{m}(\xi) = \left(-\frac{1}{\lambda} \cos(\lambda \xi) + \frac{2}{\sigma^2 \lambda^2} \sin(\lambda \xi) \xi\right) \exp\left(-\left(\frac{\xi}{\sigma}\right)^2\right) . \tag{62}$$

For the computations presented here, we chose $\varepsilon = 0.1$ and a Courant-Friedrichs-Lewy number $\mathrm{cfl}_{\Delta x} = 8$, which results in an effective CFL number of $\mathrm{cfl} = 80$ with respect to $\Delta \xi$ in the case $\varepsilon = 0.1$.

In Figure 11 the results of the simulation using the trapezoidal rule after one and five time steps are displayed. For comparison, the asymptotic solution is plotted as a dashed line. Clearly, the numerical solution does not relax to the asymptotic solution in the pressure variable. This is also true for later time steps (not shown). The results suggest that the balanced momentum field is well approximated. However, at time $t = 0$ the initial momentum field is equal to the asymptotic solution. As we have elaborated in Section 3.4, the solution of the trapezoidal rule tends to oscillate around the balanced solution. Since the deviation from the balanced solution is very small for the momentum, the non-vanishing deviations are barely visible. We will elaborate on this issue below.

The results of the simulations using the BDF(2) scheme are given in Figure 12. In this case we find that the balanced state is essentially attained already after one time step. After five time steps, the numerical solution is nearly indistinguishable from the asymptotic solution. This is the desired behavior.

Figures 13 and 14 display the results obtained with the blended schemes. For both versions, we observe the correct behavior after several time steps. In comparison with the reference schemes, the solutions after one time step are somewhere between the solutions of the trapezoidal rule and the BDF(2) scheme. However, after five time steps the solutions have relaxed to the asymptotic solution.

To show that not only the pressure variable is problematic, the simulations are repeated, but this time they start at $t = \frac{\pi}{4\omega}$. At this time the balanced state is different from the initial data in both variables. The results are shown after one and 18 time steps. As shown in Figure 15 for the trapezoidal rule there is a much bigger difference in the pressure variable, which additionally grows during the first time steps (note the different scaling in p compared to the other figures!). This time there is also a non-vanishing deviation in the momentum variable visible. Also the results obtained with the BDF(2) scheme (Figure 16) show a considerably larger deviation from the balanced state after one time step. However, after four time steps (not shown) the solution has again relaxed to the balanced state. This behavior is also obtained with the blended trapezoidal/BDF(2) scheme, as displayed in Figure 17. Here the relaxation process takes about 10 steps (not shown). On the other hand, the results from the blended trapezoidal/super-implicit scheme in Figure 18 show that this method does not
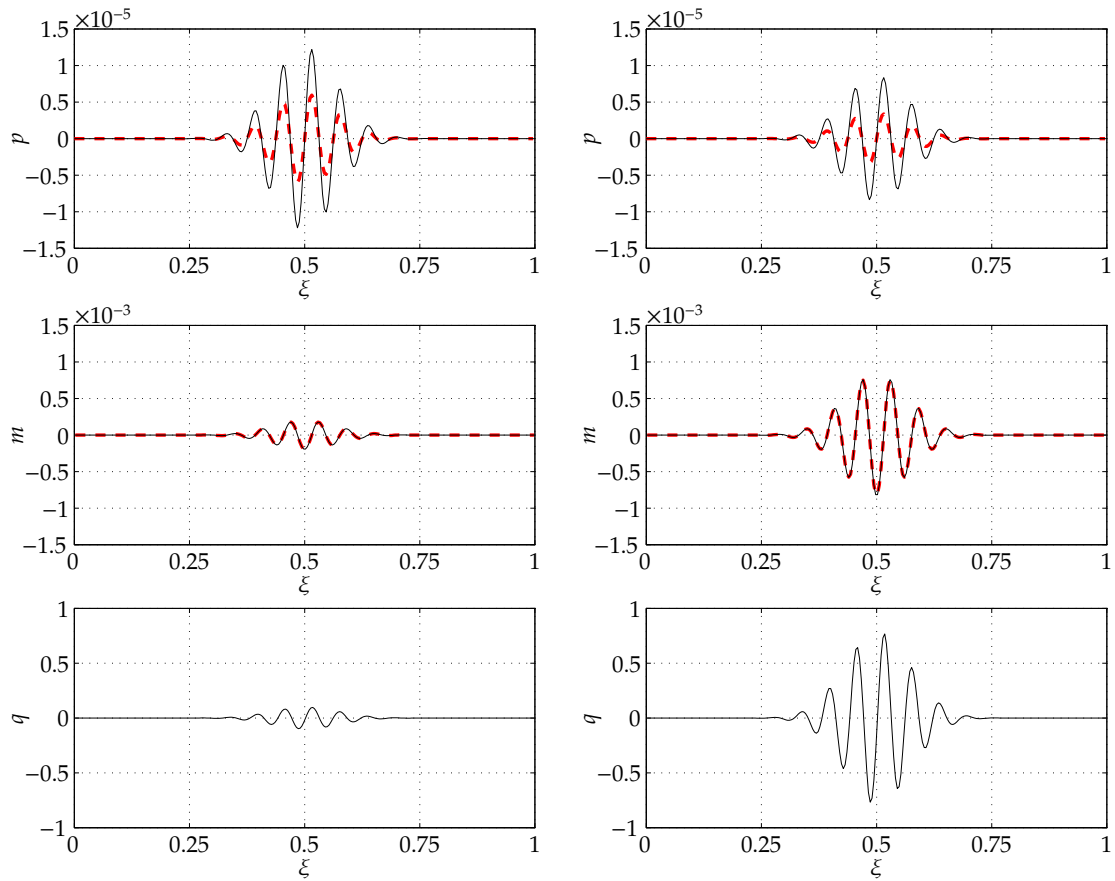
Figure 11: Numerical solution using the trapezoidal rule (black line) on a grid with 256 cells and $\mathrm{cfl} = 8$ after one (left) and five (right) time steps. Asymptotic solution is plotted as dashed lines.
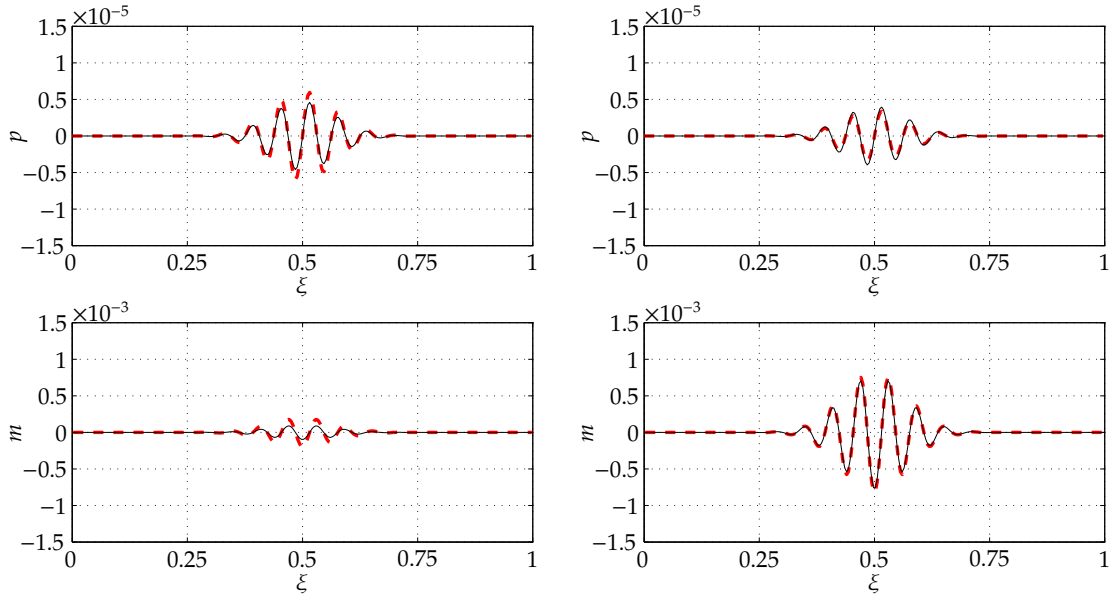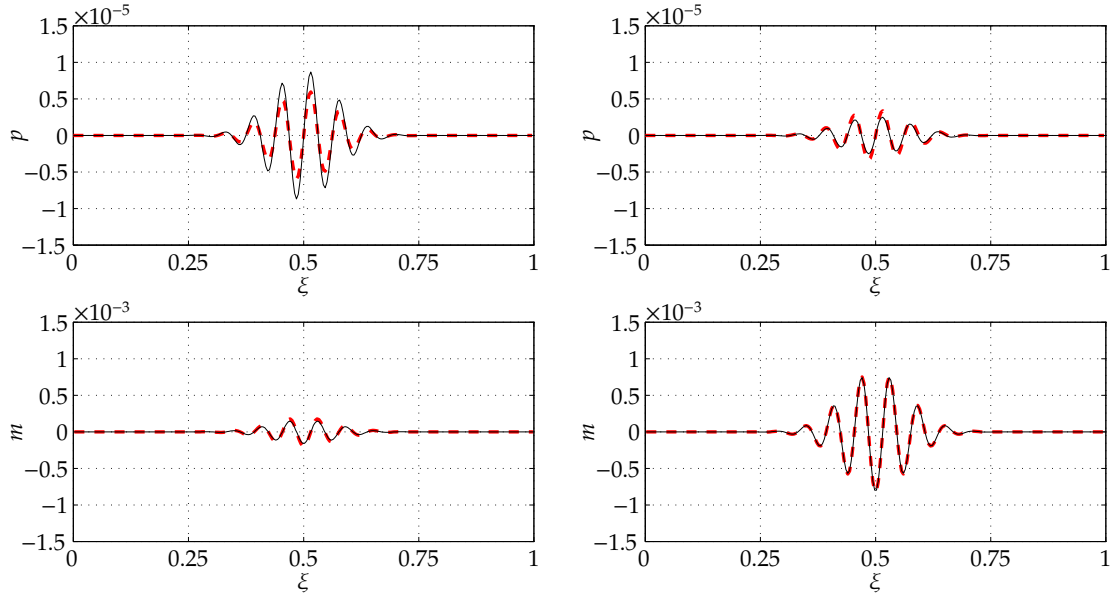
Figure 12: Numerical solution using the BDF(2) scheme (black line) on a grid with 256 cells and $\mathrm{cfl} = 8$ after one (left) and five (right) time steps. Source term as in Figure 11. Asymptotic solution is plotted as dashed lines.
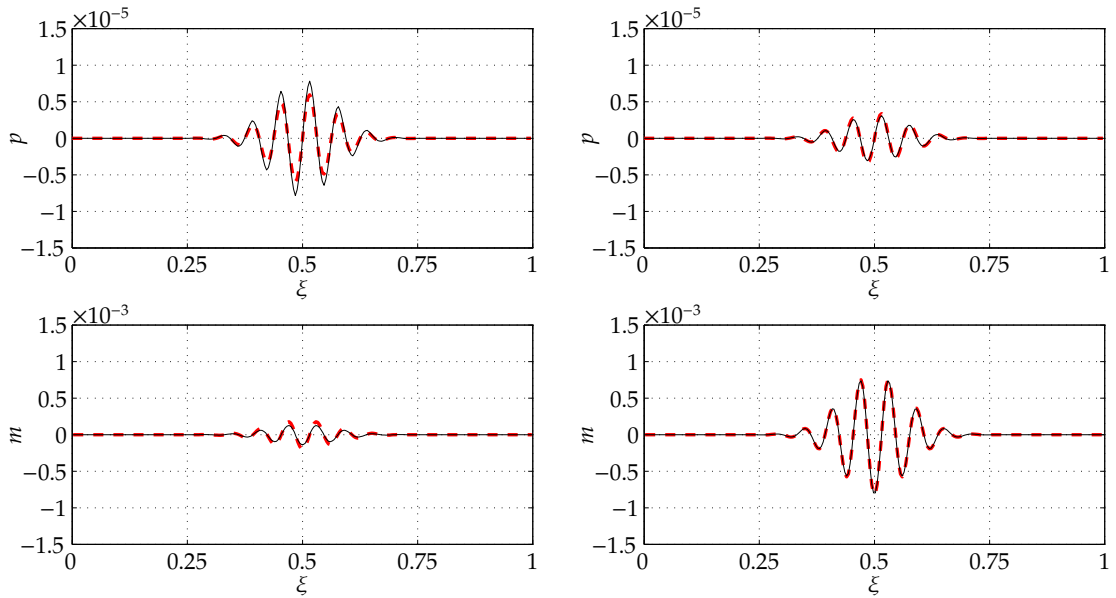
Figure 13: Numerical solution using the blended trapezoidal/BDF(2) scheme (black line) on a grid with 256 cells and $\mathrm{cfl} = 8$ after one (left) and five (right) time steps. Source term as in Figure 11. Asymptotic solution is plotted as dashed lines.

Figure 14: Numerical solution using the blended trapezoidal/super-implicit scheme (black line) on a grid with 256 cells and $\mathrm{cfl} = 8$ after one (left) and five (right) time steps. Source term as in Figure 11. Asymptotic solution is plotted as dashed lines.

have the desired property to relax to the balanced state in this case. This is due to the fact that the selected source term is localized by a Gaussian pulse, which incorporates nearly all Fourier modes. As we have stated above, the super-implicit scheme is unstable for long-wave data, and thus, one obtains the observed behavior. If the source term is of the form

$$q\left(t, \xi\right) = \sin\left(\omega\, t\right) \sin\left(\lambda(\xi - \xi_0)\right) \ , \tag{63}$$

the scheme shows relaxation to the balanced state (not shown).

6 Discussion and Conclusions

In this study, a new method for the numerical integration of the one-dimensional linear acoustic equations is introduced. It is motivated by some shortcomings of classical semi-implicit large time step numerical integration schemes applied in current atmospheric codes. The new scheme effectively eliminates freely propagating compressible short-wave components, which cannot be accurately represented at long time steps. At the same time, the dispersion and the amplitude errors for long-wave modes are minimized. In the presence of a source term that varies slowly in time but has rapid spatial variations, solutions relax to an asymptotic balanced state. In order to achieve these properties, a quasi-spectral decomposition of the data is performed using multigrid techniques, and a
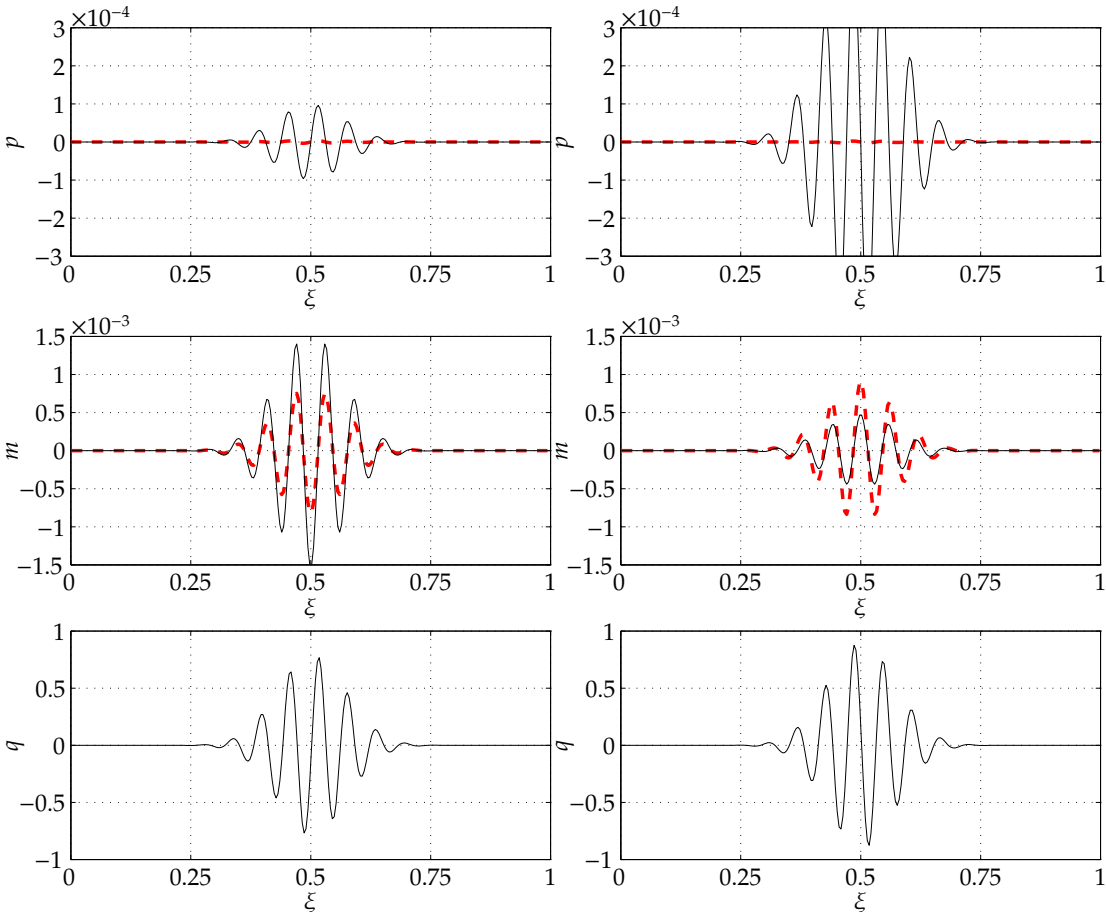
Figure 15: Numerical solution using the trapezoidal rule (black line) on a grid with 256 cells and cfl = 8 after one (left) and 18 (right) time steps. Completely unbalanced data. Notice the different scaling in p compared to the other figures. Asymptotic solution is plotted as dashed lines.
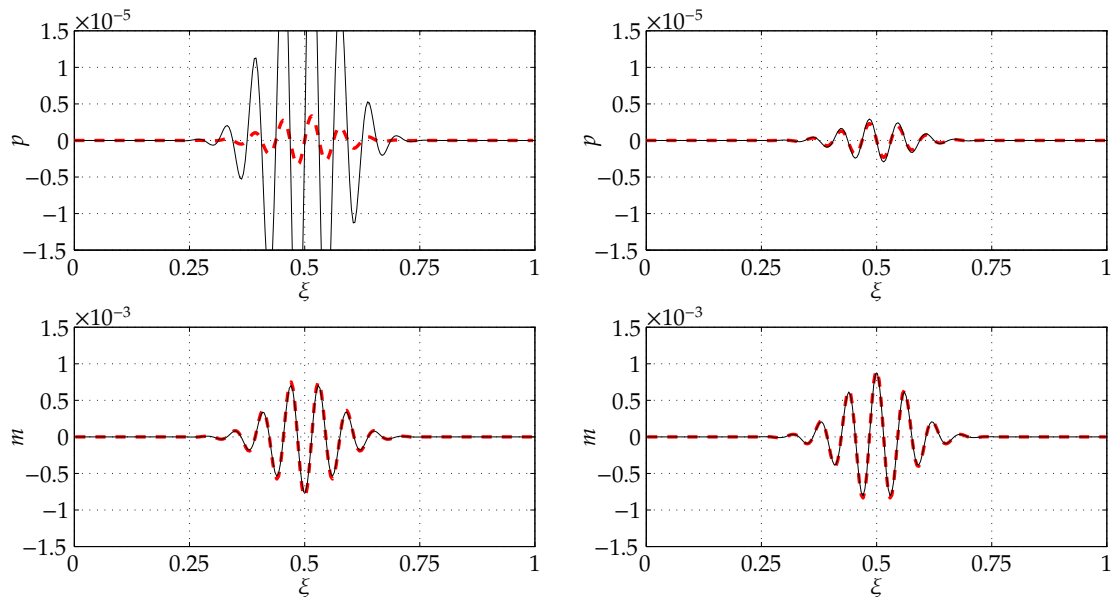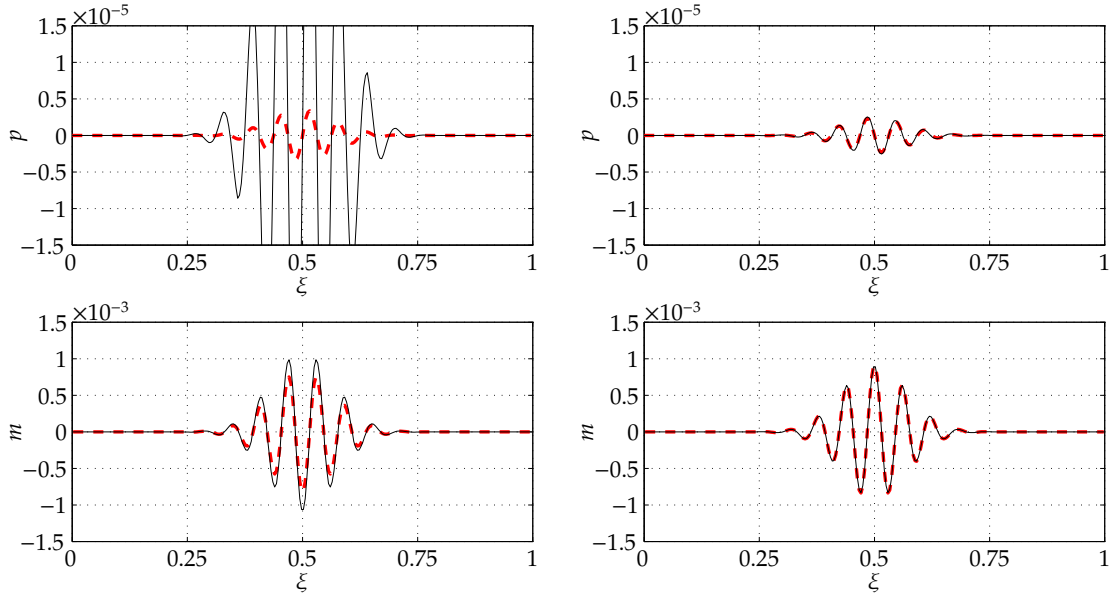
Figure 16: Numerical solution using the BDF(2) scheme (black line) on a grid with 256 cells and $\mathrm{cfl} = 8$ after one (left) and 18 (right) time steps. Completely unbalanced data. Source term as in Figure 15. Asymptotic solution is plotted as dashed lines.

scale-dependent blending of two base schemes is applied.

Two classical implicit one step methods and a new super-implicit discretization were analyzed. The discrete-dispersion relations gave insight into the dispersion and amplitude errors produced depending on the wave number and the CFL number, and the behavior of the schemes in presence of a source term was discussed. This analysis enabled us to effectively control the characteristics of the new method concerning accurate transport of long-wave and dissipation of under-resolved short-wave acoustic modes.

In contrast to most other stabilization techniques used in codes for numerical weather prediction, the new scheme is still consistent of second order accuracy. Other techniques, like off-centering, divergence damping [Skamarock and Klemp, 1992] or subgrid scale (SGS) filters either reduce the order of the scheme to first order, or are not consistent with the underlying equations. Here, we deliberately employ the truncation properties of certain "simple" schemes to achieve positive effects in terms of subgrid-scale modeling. This is in spirit of implicit Large Eddy Simulations [Grinstein *et al.*, 2007] for turbulence modeling.

As it was already mentioned in the introduction, it is still not clear how much any acoustic mode really matters in atmospheric modeling. Thus, the importance of the proposed scheme might be debatable with respect to acoustics. However, as it was shown in Klein *et al.* [2010], there is also a clear scale separation between gravity wave modes and advection, and similar problems arise in this context. We think that the
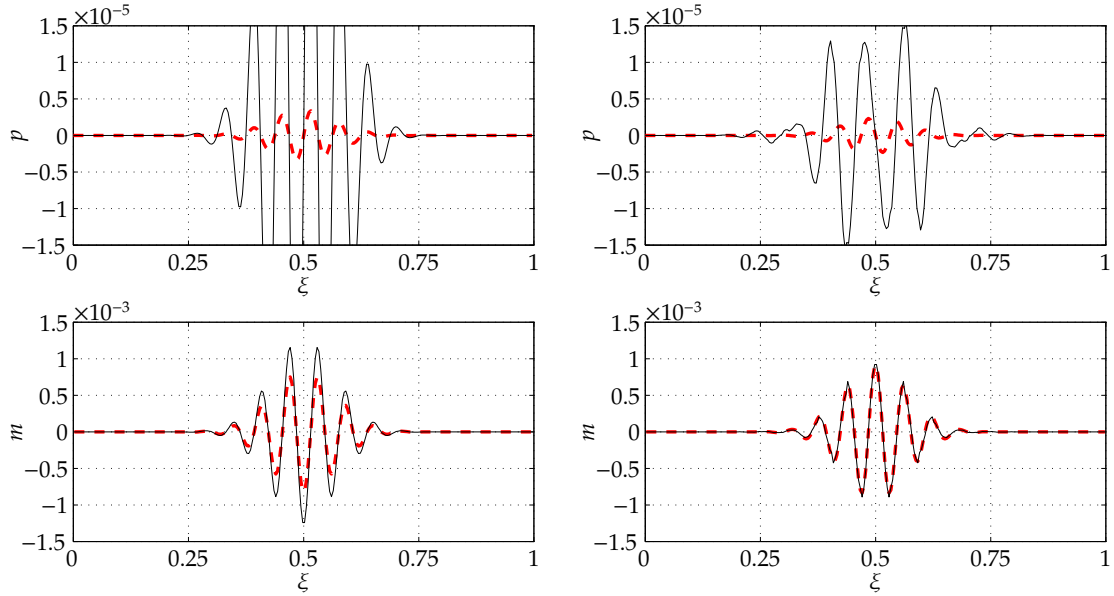
Figure 17: Numerical solution using the blended trapezoidal/BDF(2) scheme (black line) on a grid with 256 cells and $\text{cfl} = 8$ after one (left) and 18 (right) time steps. Completely unbalanced data. Source term as in Figure 15. Asymptotic solution is plotted as dashed lines.

scheme is also applicable for this issue.

The overall idea of the scheme is quite general and can likely be applied also in other contexts in which only partially resolved processes require a scale-selective numerical representation.

Some open questions remain, however. For the selection of the base schemes, mostly classical discretizations were applied so far. There might be special discretizations, which are more suitable for the particular purpose than the presented schemes. A first try in this direction was the super-implicit scheme. However, the results from the test case with slow, short-wave source term suggest that this choice is not optimal yet. Furthermore, the weighting function μ_ν for the blending of the base schemes was chosen rather ad-hoc thus far, and more judicious choices aiming at optimization of the dispersion and damping effects are conceivable.

Another important issue is the efficient implementation of the described method. Especially, when applied to 2D or 3D problems, fast algorithms such as multigrid methods must be at hand. The authors are currently working on the development of such methods with the aim of using the scale decomposition simultaneously for the blending of time integrators and for the efficient solution or preconditioning of the linear equations resulting from the semi-implicit discretization.

Figure 18: Numerical solution using the blended trapezoidal/super-implicit scheme (black line) on a grid with 256 cells and cfl $= 8$ after one (left) and 18 (right) time steps. Completely unbalanced data. Source term as in Figure 15. Asymptotic solution is plotted as dashed lines.

Acknowledgements

Appendix

Splitting relationship between pressure and momentum

For the derivation of the splitting relationship between the pressure and momentum fields, let us consider just two grid levels. The fine grid has nodes $x_{j+1/2}$, $j = \ldots, -1, 0, 1, \ldots,$ and the coarse grid should have nodes $x_{2j+1/2}$, $j = \ldots, -1, 0, 1, \ldots$ The pressure should decompose into fine and coarse grid portions:

$$p_{j+1/2} = p_{j+1/2}^{(f)} + p_{j+1/2}^{(c)} \, . \tag{A1}$$

Using the full weighting (restriction) operator, the coarse grid portion at common grid points is given by

$$p_{2j+1/2}^{(c)} = \frac{1}{4}p_{2j-1/2} + \frac{1}{2}p_{2j+1/2} + \frac{1}{4}p_{2j+3/2} \; . \tag{A2}$$

At the other nodes, we define the coarse grid portion by linear interpolation:

$$
\begin{aligned}
p_{2j+3/2}^{(c)} &= \frac{1}{2}\left(p_{2j+1/2}^{(c)} + p_{2j+5/2}^{(c)}\right) \\
&= \frac{1}{8}p_{2j-1/2} + \frac{1}{4}p_{2j+1/2} + \frac{1}{4}p_{2j+3/2} + \frac{1}{4}p_{2j+5/2} + \frac{1}{8}p_{2j+7/2} \; .
\end{aligned}
\tag{A3}
$$

The fine grid portion can then be computed by relation (A1). We obtain

$$
\begin{aligned}
p_{2j+1/2}^{(f)} &= p_{2j+1/2} - p_{2j+1/2}^{(c)} \\
&= -\frac{1}{4}p_{2j-1/2} + \frac{1}{2}p_{2j+1/2} - \frac{1}{4}p_{2j+3/2}
\end{aligned}
\tag{A4}
$$

and

$$
\begin{aligned}
p_{2j+3/2}^{(f)} &= p_{2j+3/2} - p_{2j+3/2}^{(c)} \\
&= -\frac{1}{8}p_{2j-1/2} - \frac{1}{4}p_{2j+1/2} + \frac{3}{4}p_{2j+3/2} - \frac{1}{4}p_{2j+5/2} - \frac{1}{8}p_{2j+7/2} \; .
\end{aligned}
\tag{A5}
$$

As stated above, we would like to compute the resulting splitting for $\partial p / \partial x$ to obtain the proper splitting for the momentum variable. For our staggered grid approach, the momentum is associated to the cells $C_j = [x_{j-1/2}, x_{j+1/2}]$, and the first derivative of the pressure is approximated by

$$\left.\frac{\partial p}{\partial x}\right|_{x_{j+1}} \approx \frac{p_{j+3/2} - p_{j+1/2}}{\Delta x} \; . \tag{A6}$$

This is simply split into fine and coarse grid portions

$$\frac{p_{j+3/2} - p_{j+1/2}}{\Delta x} = \frac{p_{j+3/2}^{(f)} - p_{j+1/2}^{(f)}}{\Delta x} + \frac{p_{j+3/2}^{(c)} - p_{j+1/2}^{(c)}}{\Delta x} \; , \tag{A7}$$

and we obtain, by the relations (A2) to (A5),

$$
\begin{aligned}
\frac{p_{j+3/2}^{(f)} - p_{j+1/2}^{(f)}}{\Delta x} = &\left(\frac{p_{j+3/2} - p_{j+1/2}}{\Delta x}\right) - \\
&\left(\frac{1}{8}\frac{p_{j+1/2} - p_{j-1/2}}{\Delta x} + \frac{3}{8}\frac{p_{j+3/2} - p_{j+1/2}}{\Delta x} + \right. \\
&\left. \frac{3}{8}\frac{p_{j+5/2} - p_{j+3/2}}{\Delta x} + \frac{1}{8}\frac{p_{j+7/2} - p_{j+5/2}}{\Delta x}\right)
\end{aligned}
\tag{A8}
$$

and

$$\frac{p_{j+3/2}^{(c)} - p_{j+1/2}^{(c)}}{\Delta x} = \frac{1}{8}\frac{p_{j+1/2} - p_{j-1/2}}{\Delta x} + \frac{3}{8}\frac{p_{j+3/2} - p_{j+1/2}}{\Delta x} + \frac{3}{8}\frac{p_{j+5/2} - p_{j+3/2}}{\Delta x} + \frac{1}{8}\frac{p_{j+7/2} - p_{j+5/2}}{\Delta x} \tag{A9}$$

Associating $(p_{j+3/2} - p_{j+1/2})/\Delta x$ with m_{j+1}, we obtain the splitting

$$m_{j+1} = m_{j+1}^{(f)} + m_{j+1}^{(c)} \tag{A10}$$

with

$$m_{j+1}^{(c)} = \frac{1}{8}m_j + \frac{3}{8}m_{j+1} + \frac{3}{8}m_{j+2} + \frac{1}{8}m_{j+3} \tag{A11}$$

and

$$m_{j+1}^{(f)} = m_{j+1} - m_{j+1}^{(c)} \tag{A12}$$

for the momentum field. This results in the restriction and prolongation operators

$$R^{(\nu)} = \frac{1}{8}\begin{bmatrix} 1 & 3 & 3 & 1 \end{bmatrix} \quad \text{and} \quad P^{(\nu)} = \begin{bmatrix} 1 & 1 \end{bmatrix}. \tag{A13}$$

References

Courant, R., K. O. Friedrichs, and H. Lewy (1928), Über die partiellen Differenzengleichungen der mathematischen Physik, *Mathematische Annalen* **100**, 32–74.

Davies, T., A. Staniforth, N. Wood, and J. Thuburn (2003), Validity of anelastic and other equation sets as inferred from normal-mode analysis, *Quarterly Journal of the Royal Meteorological Society* **129**, 2761–2775, DOI: 10.1256/qj.02.1951.

Deuflhard, P., and F. Bornemann (2002), *Scientific Computing with Ordinary Differential Equations*, vol. 42 of *Texts in Applied Mathematics*, Springer.

Dubois, T., F. Jauberteau, and R. Temam (2004), *Encyclopedia of Computational Mechanics*, John Wiley & Sons, Ltd, chap. Dynamic Multilevel Methods and Turbulence, DOI: 10.1002/0470091355.ecm059.

Dubois, T., F. Jauberteau, R. Temam, and J. Tribbia (2005), Multilevel schemes for the shallow water equations, *Journal of Computational Physics* **207**, 660–694, DOI: 10.1016/j.jcp.2005.01.025.

Durran, D. R. (1989), Improving the Anelastic Approximation, *Journal of the Atmospheric Sciences* **46**, 1453–1461, DOI: 10.1175/1520-0469(1989)046<1453:ITAA>2.0.CO;2.

Durran, D. R. (2010), *Numerical Methods for Fluid Dynamics: With Applications to Geophysics*, no. 32 in Texts in Applied Mathematics, Springer, 2nd edn..

Fukushima, T. (1999), Super Implicit Multistep Methods, in: H. Umehara (ed.), *31st Symposium on Celestial Mechanics*, Kashima Space Research Center, Ibaraki, Japan, 343–366.

Grabowski, W. W. (1998), Toward Cloud Resolving Modeling of Large-Scale Tropical Circulations: A Simple Cloud Microphysics Parameterization, *Journal of the Atmospheric Sciences* **55**, 3283–3298, DOI: 10.1175/1520-0469(1998)055<3283:TCRMOL>2.0.CO;2.

Grinstein, F. F., L. G. Margolin, and W. J. Rider (2007), *Implicit Large Eddy Simulation*, Cambridge University Press, DOI: `10.1017/CBO9780511618604`.

Hairer, E., C. Lubich, and G. Wanner (2006), *Geometric Numerical Integration: Structure-Preserving Algorithms for Ordinary Differential Equations*, vol. 31 of *Springer Series in Computational Mathematics*, Springer, 2nd edn..

Klein, R. (2009), Asymptotics, structure, and integration of sound-proof atmospheric flow equations, *Theoretical and Computational Fluid Dynamics* **23**, 161–195, DOI: `10.1007/s00162-009-0104-y`.

Klein, R., U. Achatz, D. Bresch, O. M. Knio, and P. K. Smolarkiewicz (2010), Regime of Validity of Soundproof Atmospheric Flow Models, *Journal of the Atmospheric Sciences* **67**, 3226–3237, DOI: `10.1175/2010JAS3490.1`.

Lipps, F. B., and R. S. Hemler (1982), A Scale Analysis of Deep Moist Convection and Some Related Numerical Calculations, *Journal of the Atmospheric Sciences* **39**, 2192–2210, DOI: `10.1175/1520-0469(1982)039<2192:ASAODM>2.0.CO;2`.

Ohfuchi, W., H. Nakamura, M. Yoshioka, T. Enomoto, K. Takaya, X. Peng, S. Yamane, T. Nishimura, Y. Kurihara, and K. Ninomiya (2004), 10-km mesh meso-scale resolving simulations of the global atmosphere on the Earth Simulator: Preliminary outcomes of AFES (AGCM for the Earth Simulator), *Journal of the Earth Simulator* **1**, 8–34.

Schneider, T., N. Botta, K. J. Geratz, and R. Klein (1999), Extension of Finite Volume Compressible Flow Solvers to Multi-dimensional, Variable Density Zero Mach Number Flows, *Journal of Computational Physics* **155**, 248–286, DOI: `10.1006/jcph.1999.6327`.

Skamarock, W. C., and J. B. Klemp (1992), The Stability of Time-Split Numerical Methods for the Hydrostatic and the Nonhydrostatic Elastic Equations, *Monthly Weather Review* **120**, 2109–2127, DOI: `10.1175/1520-0493(1992)120<2109:TSOTSN>2.0.CO;2`.

Smolarkiewicz, P. K., and A. Dörnbrack (2008), Conservative integrals of adiabatic Durran's equations, *International Journal for Numerical Methods in Fluids* **56**, 1513–1519, DOI: `10.1002/fld.1601`.

Trottenberg, U., C. Oosterlee, and A. Schüller (2001), *Multigrid*, Academic Press.

Vater, S., and R. Klein (2009), Stability of a Cartesian grid projection method for zero Froude number shallow water flows, *Numerische Mathematik* **113**, 123–161, DOI: `10.1007/s00211-009-0224-8`.